Exploring the multifunctionality of $K_3V_2(PO_4)_3$/C nanocomposites: advanced cathode for potassium-ion batteries for e-vehicles with environmental and biomedical applications

M. Gnanaprakash [a,*], S.P. Mangaiyarkarasi [a], R. Gandhi Raj [b], D. Periyaazhagar [c]
[a] *Department of Electrical and Electronics Engineering, University College of Engineering, Panruti. Tamilnadu, India. 607106*
[b] *Department of Electrical and Electronics Engineering, University College of Engineering - BIT Campus, Tiruchirappalli, Tamilnadu, India. 620024*
[c] *Department of Electrical and Electronics Engineering, Krishnasamy College of Engineering and Technology, Cuddalore, Tamil Nadu, India. 607109*

$K_3V_2(PO_4)_3$/C is a gorgeous material for KIBs because of impressive voltage, good stability, fast K^+ diffusion, and improved conductivity from carbon modification. Here, a three-dimensionally active network nanocomposite of $K_3V_2(PO_4)_3$/C—has been intended, and established. The materials were examined using XRD, SEM and XPS to elucidate their structural, morphological, and elemental composition. Ideal cathode samples for K-ion based storage devices (KIBs) and photocatalytic ingredients in the breakdown of 2 chlorophenol (2-CP) may be the obtained $K_3V_2(PO_4)_3$/C nanocomposites. At 100 mAg^{-1} one may get a steady capacity of 121 $mAhg^{-1}$. After 2000 cycling performance, 96.3% of the ability may still be kept despite a elevated current intensity of 2000 mAg^{-1}. Furthermore, under comparable conditions of testing, $K_3V_2(PO_4)_3$/C composite shown remarkable degrading efficiency (98.5%) and rate constant (0.09761 min^{-1}) to CR dye than against RhB dye. Additionally, performed were the functions of pH and free radical investigations. Moreover, this new $K_3V_2(PO_4)_3$/C nanocomposite will have enormous capacity to be applied to other industries, such particular catalysis, hydrogen generation and other energy production uses, because of cheap cost, ecological sustainability as well as abundance of origin.

(Received May 7, 2025; Accepted August 1, 2025)

Keywords: KIBs, $K_3V_2(PO_4)_3$/C, Porous carbon, Environmental applications, Energy storage

1. Introduction

The growing emphasis on sustainable and high-efficiency energy storage technologies has spurred the exploration of innovative battery systems, particularly to meet the requirements of electric vehicle (EV) applications. While lithium-ion batteries (LIBs) remain the leading choice for commercial applications, the demand for alternative battery technologies has been sparked by issues about higher prices, dwindling lithium materials, and related environmental effects [1–4]. As a feasible energy storage option, potassium-ion batteries (KIBs) are receiving attention as a result of their widespread availability, low production cost, and electrochemical properties that are comparable to those of lithium-ion batteries (LIBs). When comparing potassium (K) to lithium (Li), potassium has more enticing benefits in terms of its origin and supplies. Particularly, K has a redox capability that is more similar to Li than to sodium. Furthermore, due to K^+'s better mobility over Li^+ and Na^+, potassium-ion batteries (KIBs) may increase rate reliability K^+ ions' rapid mobility and comparatively low redox potential make KIBs ideal next-generation storage platforms for high-demand power systems [5-7]. Nevertheless, the challenge of achieving high energy density, prolonged cycling stability, and exceptional charge-discharge behavior persists, underscoring the necessity of the development of more efficient electrode materials. Recently, significant attention has been devoted to identifying and optimizing various cathode materials that can effectively support the electrochemical demands of potassium-ion batteries. Among the promising candidates,

* Corresponding author: gnanaprakash.phd@gmail.com
https://doi.org/10.15251/DJNB.2025.203.883

compounds such as Prussian blue, $KTi_2(PO_4)_3$, $6FeSO_4F_{14}$, $FePO_4$, and $K_{0.7}Fe_{0.5}Mn_{0.5}O_2$ have attracted significant interest due to their favorable structural frameworks, ability to accommodate K^+ ions, and stable cycling performance. These materials are being thoroughly investigated for their potential to enhance capacity retention, rate capability, and overall efficiency, thereby contributing to the advancement of next-generation potassium-based energy storage systems. [8-11]. Literature studies reported that significant notable improvements have been realized in the design of vanadium compounds with strong electrochemical activity and various changeable valence for chemical energy retention [12]. Vanadium-based polyanionic compounds have showed tremendous promise for usage in KIB cathodes because of their significant redox capabilities, adjustable valence states, and outstanding architectural durability [13-15]. Potassium vanadium phosphate ($K_3V_2(PO_4)_3$) (PVP) is a promising cathode candidate because of its impressive ionic activity, efficient electrical pathways, and heat tolerance. This is mainly due to the high redox potential, the increased electrical activity of different vanadium values and the remarkable thermal robustness brought about by the inductive effect of $PO4^{3-}$ [16-20]. PVP has interesting properties, but its inherent low electronic conductivity and rate capability make it impractical. It has been demonstrated that incorporating a conductive carbon matrix is an effective strategy to overcome these limitations [21-23]. The incorporation of carbon coatings is a common method for improving the performance of potassium-ion batteries (KIBs). These coatings are essential for promoting ion diffusion, stabilizing structural integrity, and enabling efficient electron conduction. Various scientific efforts highlight the effectiveness of merging $K_3V_2(PO_4)_3$ (PVP) with conductive carbon matrices substantially enhances both cycling durability and rate capability [24–26]. For instance, Xu et al. created a 3D PVP/carbon composite that operated within the potential span of 3.6–3.9 V. Nevertheless, it exhibited limited tolerance for large current densities limited to maximum of 200 mA g^{-1} [27]. In the same vein, Liu's team's research indicated that their PVP/C composite had a electrochemical ability of 31 mAh g^{-1} at 15 mA g^{-1} [28]. These subpar electrochemical performances are likely due to insufficient carbon coverage, which leads to exposed active sites and large, micron-scale PVP particles. Therefore, to engineer high-performance cathode materials suitable for potassium-ion batteries, especially in real-world applications like electric vehicles, it is essential to minimize particle dimensions and achieve homogeneous dispersion within a conductive carbon matrix. Additional research should concentrate on the improvement of electrode–electrolyte compatibility and the refinement of synthesis strategies.

Furthermore, $K_3V_2(PO_4)_3$/C nanocomposites are expected to exhibit multifunctional properties suitable for biomedical, environmental, and electrochemical energy conversion systems. Their mesoporous structure with enlarged surface area and hierarchical porous structure enhance their potential for use in biomedical and catalytic fields [29-32]. The development of advanced materials for contaminant degradation, water purification, and sustainable energy conversion is now a critical global concern, as environmental protection has become a critical issue. The light-driven catalytic performance of $K_3V_2(PO_4)_3$ integrated with carbon frameworks has shown remarkable potential, enabled effective breakdown of organic contaminants when exposed to visible light. Recent research has demonstrated that photocatalytic materials are instrumental in the reduction of environmental contaminants by initiating the formation of reactive oxidative intermediates that degrade harmful substances [33-34]. More recently, the demand for biocompatible and effective therapeutic materials in biomedical applications is increasing. Vanadium-based compounds demonstrate superior antioxidant capabilities, effectively neutralizing oxidizing reactive species and preventing oxidizing cellular damage [35]. Antioxidants are essential in reducing diseases related to oxidative damage conditions cancer, neurological disorders and cardiovascular diseases. Recent investigations have underscored the promise of vanadyl/rGO composites in biological applications, illustrating their ability to serve as both therapeutic agents and diagnostic instruments [36]. The capacity of these nanocomposites to function as photocatalysts and antioxidants highlights their versatility and multifunctionality, rendering them appropriate for advanced environmental and medicinal applications. Reactive oxygen species that decompose deleterious compounds.

Based on these considerations, this study investigates the fabrication and versatile functionality of a newly developed $K_3V_2(PO_4)_3$/carbon nanocomposite, aiming to utilize it as a high-performance cathode for potassium-ion batteries in electric vehicles, along with potential applications in environmental remediation and biomedical technologies. The optimized

nanostructure, thin carbon coating and unique 3D porous architecture significantly enhance electrochemical performance, ensuring superior charge–discharge efficiency and durability over prolonged use. Additionally, the composite's remarkable photocatalytic efficiency and antioxidant properties highlight its potential for pollutant degradation and biomedical applications. These advancements position $K_3V_2(PO_4)_3$/C nanocomposites as potential alternatives for eco-friendly power storage systems, environmental remediation and medical innovations.

2. Experimental section

2.1. Preparation of $K_3V_2(PO_4)_3$/C composites

The raw materials (0.4 g CH_3COOK, 0.8 g NH_4VO_3, 0.4 g $NH_4H_2PO_4$, 1.2 g $C_6H_8O_7 \cdot H_2O$) were disintegrated in 50 mL DI water using balanced ratios, then swirled at 80 °C until a jelly-like condition developed. The prepared mixture was then subjected to microwave irradiation at 1000 W for 20 min. The resulting precipitate was carefully collected and thoroughly treated repeatedly using ethanol and deionized water to remove residues and to ensure purity. After drying at 60 °C for 12 h, the samples underwent calcination at 350 °C for 4 h to complete the thermal processing. The pure and carbon-integrated materials were designated as KVP and KVP/C, respectively. Fig. 1(a) depicts an expanded schematic representation outlining the synthesis steps involved in creating the three-dimensional $K_3V_2(PO_4)_3$/C hybrid material.

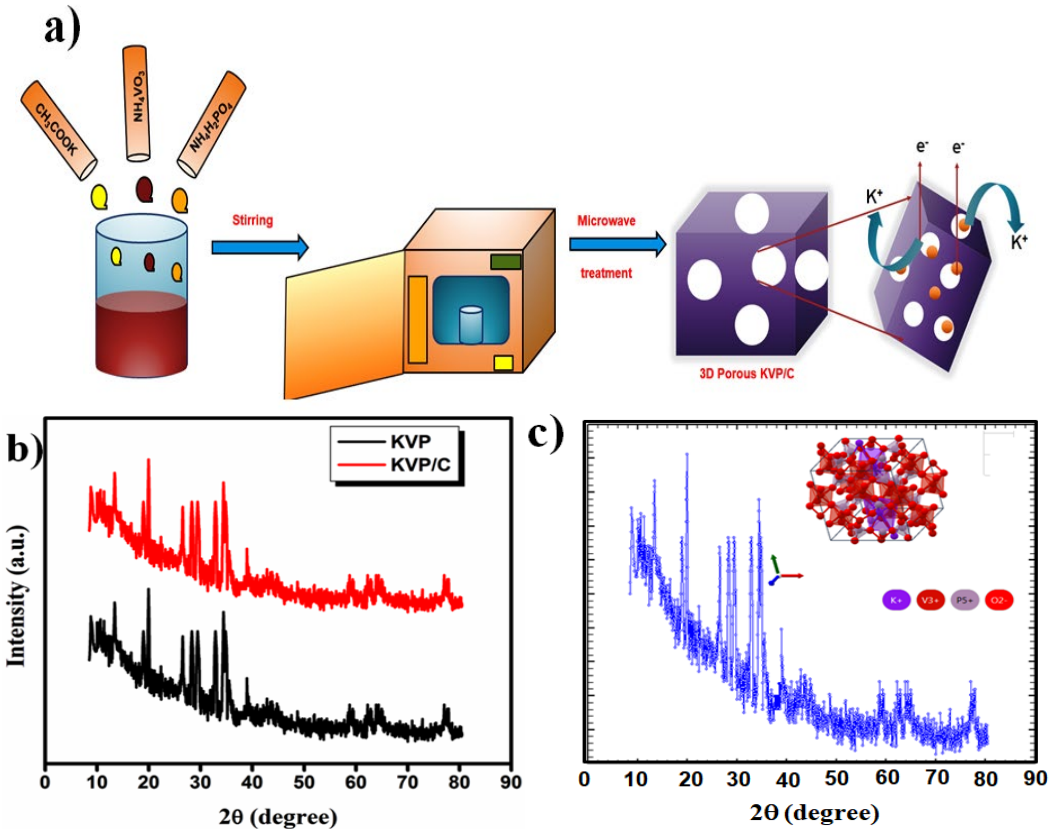

Fig. 1. (a) Graphic illustration of the KVP/C preparation route (b) Powder XRD patterns of KVP/C (c) Rietveld refinement of $K_3V_2(PO_4)_3$/C, with the inset displaying its crystal structure.

2.2. Electrochemical measurements

A glove box filled with 100% argon gas contained 2016-coin cells for electrochemical investigations. The working and counter electrodes were constructed using salt discs, while the

electrolyte comprised 1 M sodium perchlorate and 2.0 wt% PC (propylene carbonate) to enhance ionic mobility. The separator was a polypropylene (PP) microporous membrane. A homogenous slurry for the cathode electrodes was prepared by combining 70 weight percent active material, 20 weight percent acetylene black as a conductive addition, and 10 weight percent PVDF binder. NMP served as the solvent to provide uniform dispersion. The produced slurry was evenly applied to a current collector and then dried. The dried electrode film was subsequently sectioned into rectangular pieces, each possessing a surface area of 0.51 cm^2 and an estimated thickness of 0.1 mm. Mass deposition of the active substance on the electrode ranged from 3.5 to 3.9 mg/cm^2. The K/K^+ cell was subjected to galvanostatic charge–discharge measurements using a LAND CT2001A battery analyzer, which functioned within the voltage range of 1.5 to 4.0 V. Thus, the cell's electrochemical behavior was evaluated. Additionally, cyclic voltammetry (CV) and electrochemical impedance spectroscopy (EIS) analyses were performed using Auto lab PGSTAT 302N and CHI600E electrochemical analyzers, respectively, to gain a greater understanding of the electrode system's redox properties and charge-transfer resistance.

3. Results and discussion

3.1. XRD analysis

The samples were examined using XRD for phase purity and crystallinity. The corresponding pattern is demonstrated in. Fig. 1(b). As shown in figure, the XRD of the PVP and PVP/C samples are similar to the $K_3V_2(PO_4)_3$ (space group Pnna) phase that has been published earlier [37]. Due to the amorphous nature of carbon, no characteristic diffraction peaks are detected [38]. Incorporating C into KVP causes an increase in XRD peak intensities, a, b, c, and V values, as well as grain sizes of the samples. This suggests that the addition of C to PVP potentially enhances its crystallinity. Additionally, the K^+ de-embedding channel is somewhat widened by increasing the unit-cell capacity, which helps with the migration and dispersion of the big K^+ ions and helps improve the material's rate performance and cycle performance [39]. The produced PVP samples show a pure crystalline phase with the space group Pnna, as confirmed by the refinement of the XRD patterns using the Powder Cell program [40] (Fig. 1c). Furthermore, the inset in Fig. 1(c) presents the detailed crystallographic configuration of PVP. Moreover, the calculated grain sizes (18 nm for KVP and 24 nm for KVP/C) were good agreement with the SEM results.

3.2. Topographical results

Fig. 2(a) depicts the three-dimensional porous structure of the PVP/C. The goods have uniformly distributed pores, which help the electrolyte infiltrate. Fig. 2(b) shows that the pores reach depths into the materials visible, and their diameters exceed 500 nm. As shown in Fig. 2(c), transmission electron micrograph of the $K_3V_2(PO_4)_3/C$ composite shows that the carbon matrix had well-dispersed $K_3V_2(PO_4)_3$ nano-sized particles of approximately 20 nm of size. In comparison to bulk $K_3V_2(PO_4)_3$, the nanoscale dimensions of these particles substantially which may improve the electrode-electrolyte contact area, promote rapid ion diffusion and enhance reaction kinetics.

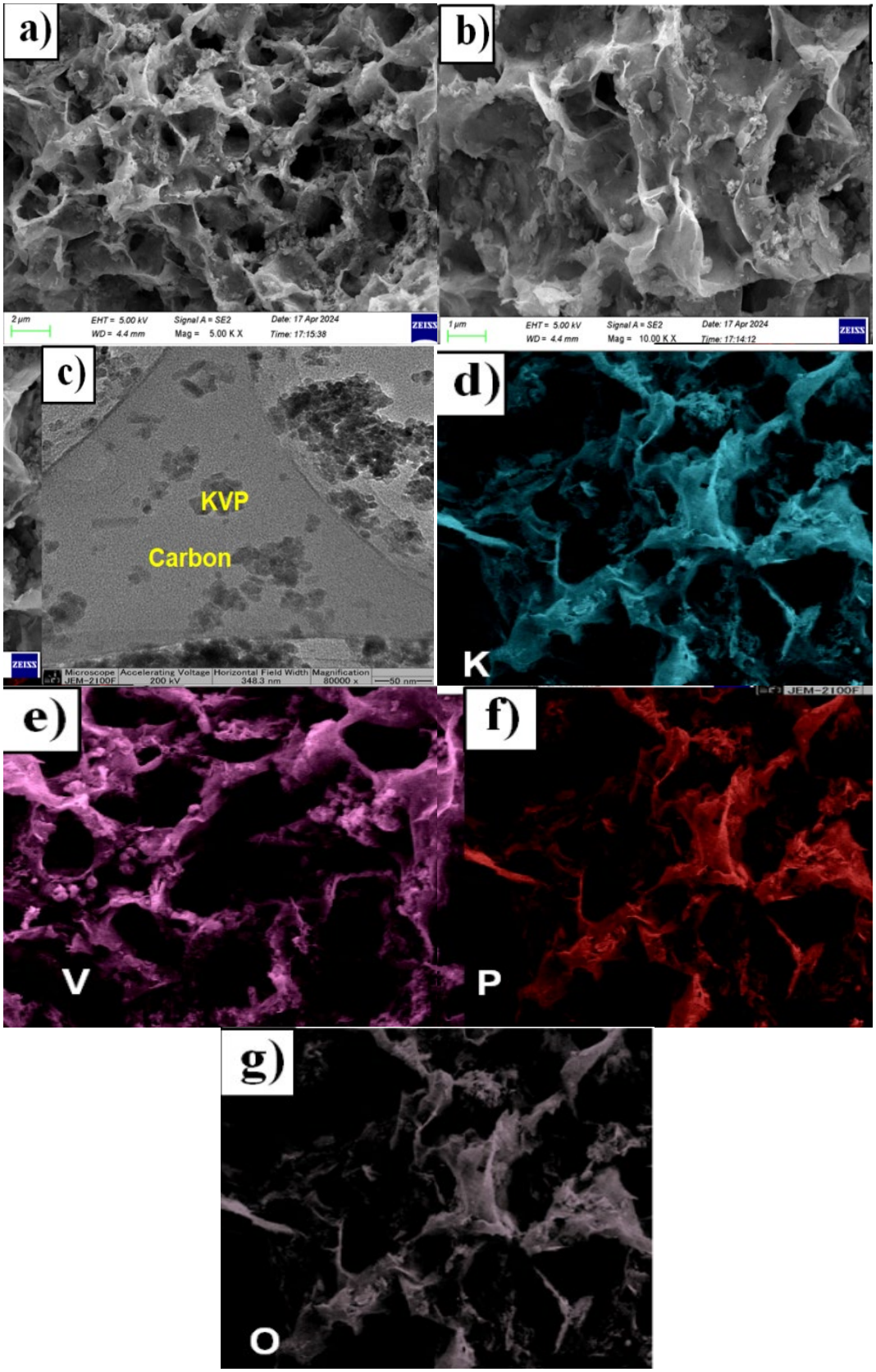

Fig. 2. (a &b) FESEM micrographs of PVP/C (c) TEM micrographs of PVP/C, Elemental mapping of (d) K (e) V (f) P and (g) O.

This nanoscale architecture enhances cycling stability and reduces charge transfer resistance, thereby improving electrochemical performance. The elemental distribution profiles in Fig. 2(d–g) reveal that potassium, vanadium, phosphorus, oxygen, and carbon are uniformly dispersed. The uniform elemental distribution confirms the successful synthesis and integration of the composite, guaranteeing steady charge-discharge performance.

3.3. Thermal analysis

Thermogravimetric analysis (TGA) was conducted on the $K_3V_2(PO_4)_3/C$ composite to evaluate its thermal stability and composition, as illustrated in Fig. 3(a). A notable mass loss was recorded in the temperature range of 350 °C to 600 °C, which can be primarily attributed to the combustion of carbon-based constituents incorporated into the composite matrix. The initial slight weight changes below 150 °C may be due to the evaporation of physically adsorbed moisture or volatile residues. The overall thermal behavior confirms the presence of carbon in the composite and supports the successful integration of the conductive phase within the KVP framework. The estimated carbon content was found to be at 28 wt%, reflecting the level of carbon incorporation in the material. The addition of carbon improves the composite's electrical conductivity and electrochemical performance by increasing electron transport while retaining structural integrity. At temperatures above 600 °C, V^{3+} oxidizes to higher oxidation states (V^{4+} or V^{5+}) in the presence of oxygen, resulting in a slight weight gain between 550 and 750 °C. This oxidation process implies a progressive transition of vanadium species, which may alter the material's electrochemical characteristics of the materials. The observed thermal behavior demonstrates that the $K_3V_2(PO_4)_3/C$ composite retains structural integrity up to 350°C before major decomposition commences. This finding is critical for practical applications since it shows the composite's thermal resistance under regular working circumstances in energy storage devices. Furthermore, the regulated carbon content maintains a balance of conductivity and thermal stability, which improves the composite's overall electrochemical performance.

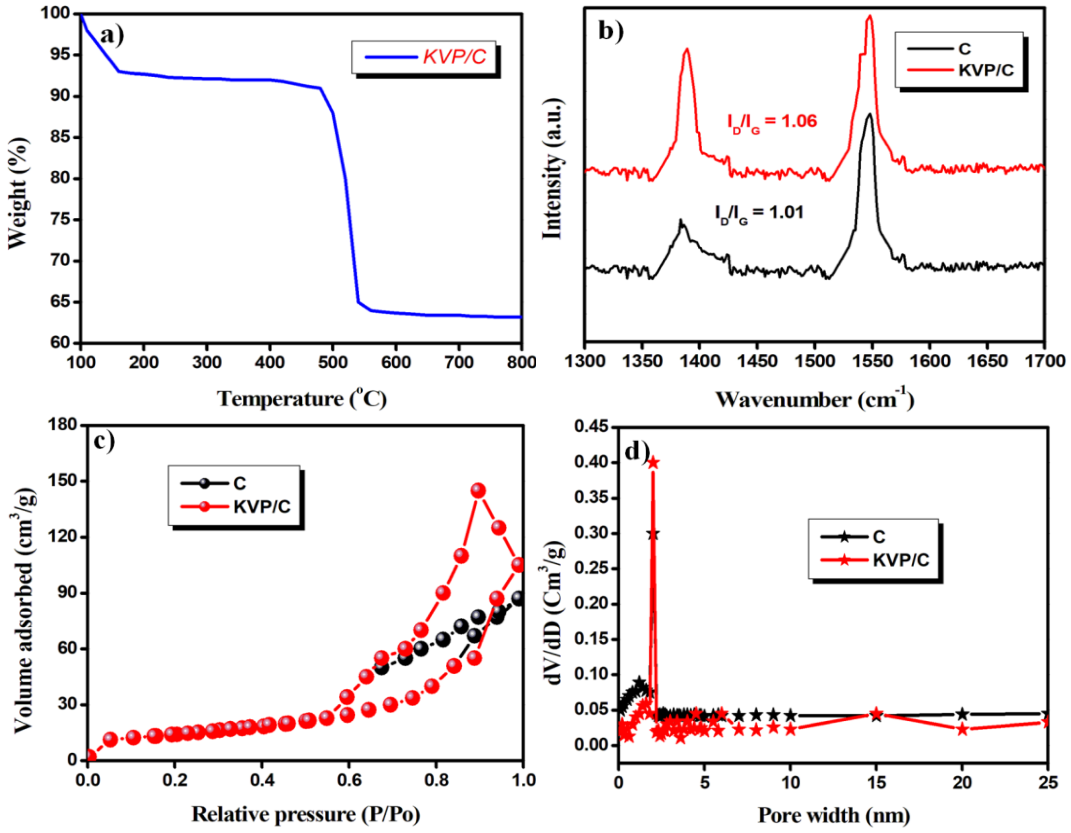

Fig. 3. (a) Thermogravimetric plot (b) Raman spectra (c) & (d) Ns isotherm and pore width curves.

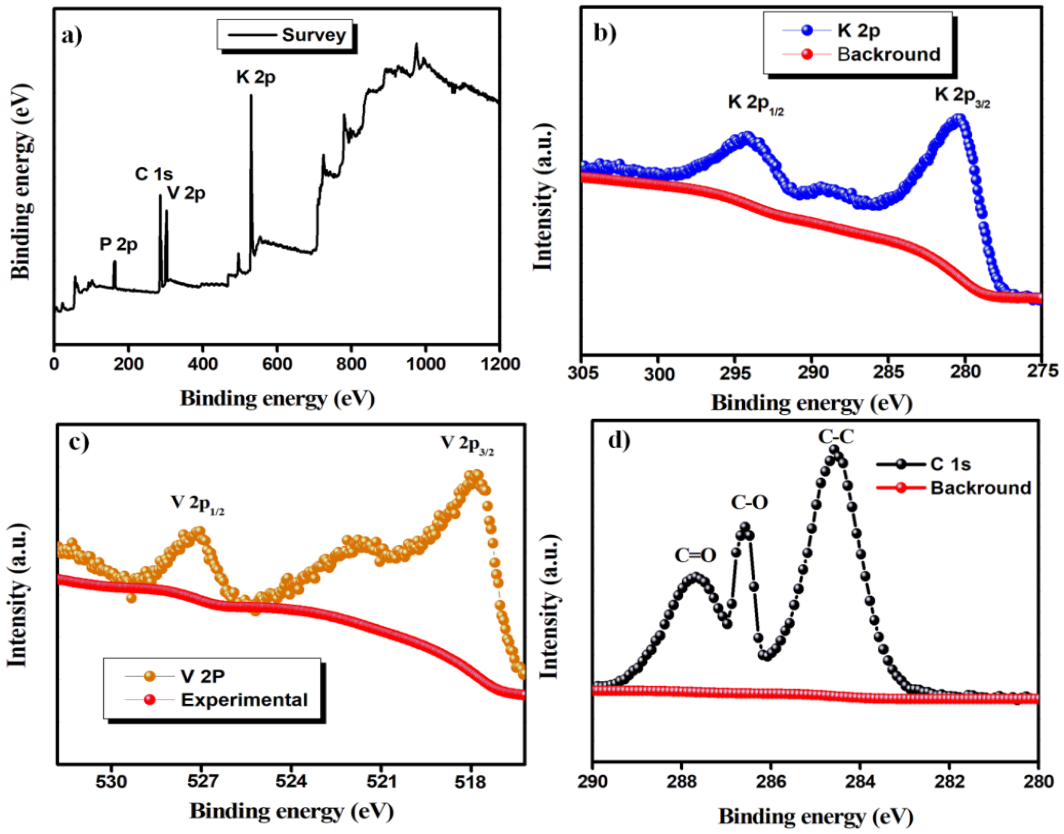

Fig. 4. the XPS results of PVP/C: (a) the survey spectrum (b-d) high-resolution core-level spectra corresponding to its elemental components.

3.4. Raman spectra analysis

Raman spectroscopy was employed to investigate the presence of graphene in the PVP/C composite, as illustrated in Fig. 3(b). The spectrum exhibited two distinctive peaks at 1353 cm^{-1} and 1579 cm^{-1}. These peaks are attributed to the D band, which is associated with disordered or defective carbon structures, and the G band, which is related to the in-plane resonance of sp^2-bonded carbon atoms [41-42]. The PVP/C sample has an intensity ratio (I_D/I_G) of 1.06, which is slightly lower than that of unadulterated carbon (1.1). This suggests a minor reduction in structural defects within the carbon framework following composite formation. This implies that the graphitic ordering has been somewhat enhanced by the thermal or chemical processing that was employed to synthesize the composite. However, the carbon matrix maintains an adequate electrical conductivity, which has the potential to improve the electrochemical behavior of the composite material, despite the minor remaining defects. The coexistence of disordered and graphitic carbon domains is confirmed by the presence of both D and G bands, which is advantageous for the equilibrium of structural support and conductivity. Furthermore, the modest decrease in the I_D/I_G ratio suggests that the carbon structure in the composite is partially restored to a more ordered graphitic phase. During electrochemical cycling, this enhanced structural order not only contributes to mechanical integrity but also enhances electronic pathways. These structural characteristics are especially advantageous in potassium-ion battery systems, as the presence of large ions can result in substantial volume changes. Therefore, the carbon network in PVP/C is essential for the efficient transport of charge and the preservation of electrode stability.

3.5. BET surface area analysis

Nitrogen adsorption-desorption isotherms were used to examine the specific surface areas of different prepared samples. The type IV behavior isotherms and well-defined hysteresis loops, which indicate mesoporous structures, were seen in both PVP and PVP/C as shown in Fig. 3(c).

During electrochemical cycling, this mesoporosity is vital for ion transport and electrolyte diffusion. According to the Brunauer-Emmett-Teller (BET) surface area study, the PVP/C composite had a far larger surface area of 67.7 $m^2 g^{-1}$ than the PVP, which had a surface area of just 32.3 $m^2 g^{-1}$. Because the conductive carbon is uniformly distributed and there is a hierarchical porous structure, the active sites are better exposed, and the electrolyte is able to make greater contact, leading to this improvement [43-48]. In addition, the composite materials mostly had pore sizes ranging from 2 to 6 nm, which is within the mesoporous range, according to the pore size distribution study (Fig. 3d). Such pore sizes are optimal for improving ion diffusion kinetics and shortening the transport pathways during charge–discharge processes. Overall, the increased surface area and suitable porosity provide a favorable architecture for boosting electrochemical activity, making the PVP/C composite highly suitable for energy storage applications.

3.6. XPS analysis

The elemental composition and oxidation states of the PVP/C nanocomposite were thoroughly analyzed by X-ray photoelectron spectroscopy (XPS), elucidating the surface chemistry of the material. The broad-spectrum investigation (Fig. 4a) validated the existence of K, V, P, O, and C, all of which are essential to the composition of the synthesized hybrid. This thorough scan indicates the effective integration of these components into the composite throughout the synthesis process. A comprehensive examination of the individual components was conducted utilizing high-resolution XPS spectra. Figure 4(b) illustrates a distinct pair of peaks for potassium at roughly 292.2 eV and 295.0 eV, corresponding to K $2p_{3/2}$ and K $2p_{1/2}$, respectively. The measured spin–orbit splitting of around 2.8 eV corresponds with the anticipated binding energy separation for K^+ ions, hence validating the oxidation state of potassium in the sample. The electronic state of vanadium was analyzed in the V 2p area (Fig. 4c), revealing two distinct peaks at about 515.5 eV and 525.0 eV, corresponding to V $2p_{3/2}$ and V $2p_{1/2}$, respectively. The lack of satellite peaks and the binding energy locations indicate that vanadium is mostly in the +5-oxidation state (V^{5+}), implying a stable oxidation environment without signs of mixed valence species like V^{4+} [49]. The high-resolution C 1s spectra, depicted in Fig. 4(d), exhibited peaks corresponding to carbon species, therefore corroborating the integration of conductive carbon into the composite. These peaks often signify various carbon bonding conditions, such as graphitic carbon and oxygenated functionality, which indicate partial surface oxidation and facilitate the development of a hybrid structure. The XPS results confirm the successful synthesis of the $K_3V_2(PO_4)_3$/C nanocomposite, demonstrating a uniform distribution and good integration of the carbon network inside the crystalline structure. This carbon framework increases the electrical conductivity of the material and stabilizes the composite structure, which is crucial for its performance in energy storage applications. The evident existence of K, V, P, O, and C in their anticipated oxidation states further corroborates the chemical homogeneity and structural integrity of the synthesized material.

3.7. Electrochemical performance

The cyclic voltammetry (CV) and differential capacity (dq/dV) profiles of both PVP and its carbon coated hybrids are illustrated in Fig. 5, which provides a perspective on their redox behavior. The reversible electrochemical reactions associated with potassium-ion insertion and extraction are reflected in the distinct anodic and cathodic peaks of both samples. Two distinct anodic peaks are apparent in the KVP/C composite at 1.52 V, 3.60 V respectively, while the relevant cathodic peaks are located at 1.74 V, 3.66 V respectively. The composite's electrochemical activity is underscored by the well-defined peaks, which confirm the involvement of multiple redox couples. In comparison to the pristine PVP sample, the PVP/C composite exhibits enhanced electrochemical kinetics, as evidenced by its broader CV curves and higher peak intensities.

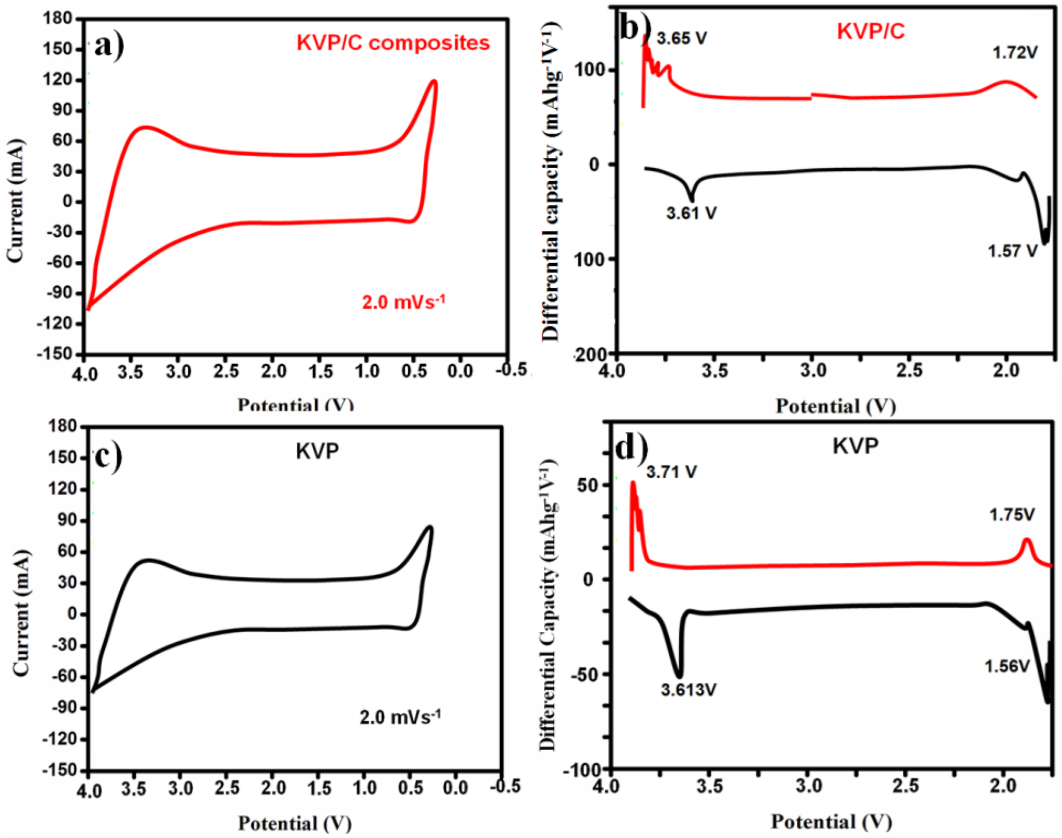

Fig. 5. Cyclic voltammograms plot of (a) PVP (c)PVP/C; K/K+. dq/dv plots of (b) PVP (d)PVP/C.

This enhancement is predominantly due to the conductive carbon matrix, which facilitates quicker electron transport and enhanced ion mobility throughout the electrode. Furthermore, the presence of a three-dimensional porous architecture facilitates the efficient transmission of charge and the penetration of electrolytes, resulting in a superior electrochemical response. The $K_3V_2(PO_4)_3$/C electrode exhibits favorable charge storage dynamics as a result of electrochemical profiling. Both the CV plot and the differential capacity (dq/dV) curve exhibit prominent features, which indicate improved reaction kinetics and increased active material utilization. Additionally, the CV plot demonstrates a broader circumscribed area. The porous carbon framework facilitates accelerated ion diffusion and reduced internal resistance, which are the causes of this enhanced behavior. At a current density of 100 mA g^{-1}, Fig. 6(a) illustrates the charge–discharge profile, which is characterized by two distinct voltage regions that are centred around 1.6 V and 3.6 V. These voltage regions are consistent with vanadium redox transitions and correspond to sequential potassium ion intercalation and deintercalation processes. The composite's high degree of structural robustness and reversibility during cycling is confirmed by the significant accord between CV and GCD measurements. The carbon-integrated PVP architecture is well-suited for the implementation in advanced potassium-ion storage systems, as it maintains electrical continuity throughout the cycling process and supports efficient redox activity, as indicated by these electrochemical responses.

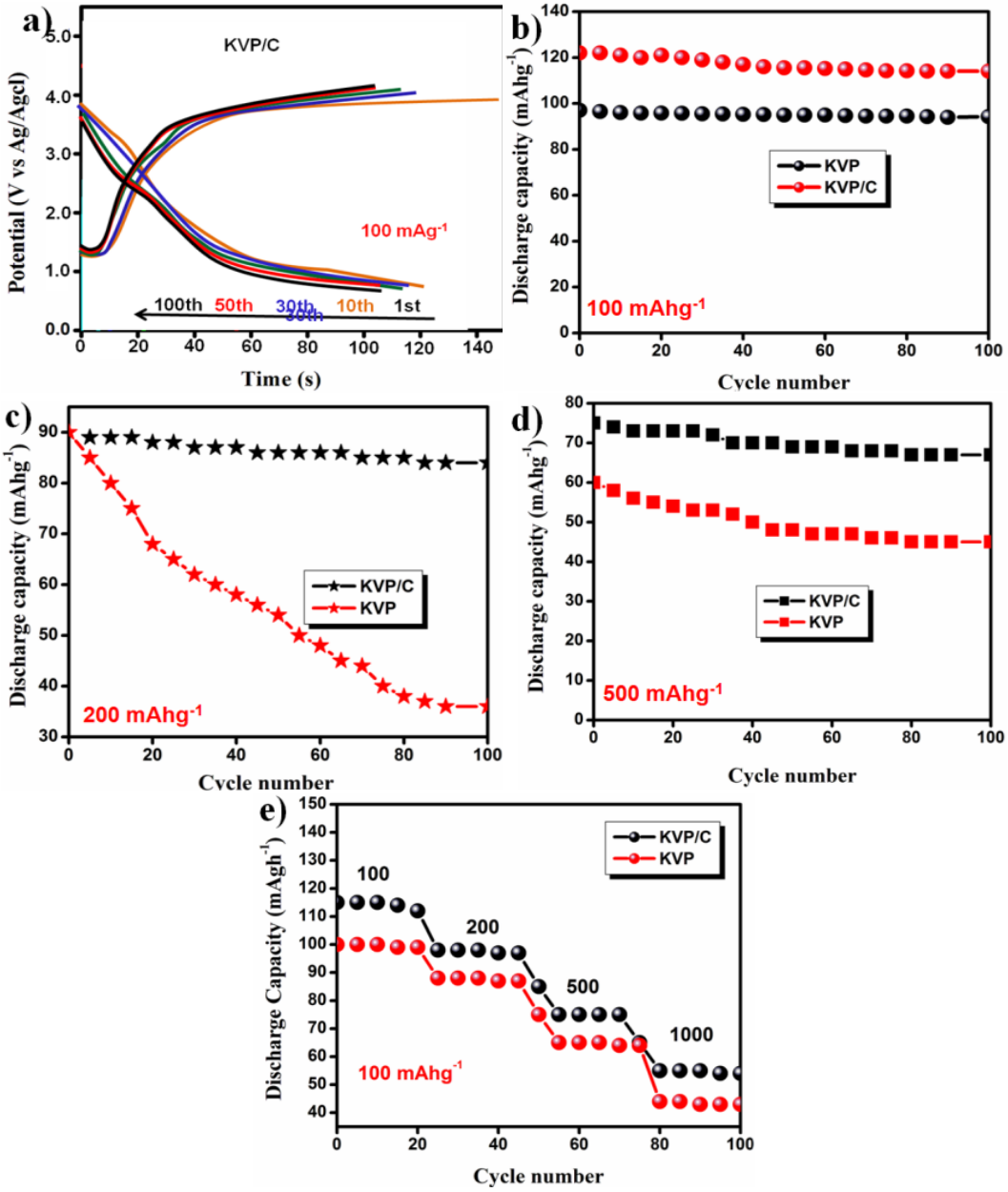

Fig. 6. (a) GCD at 100 mAg −1 (b-d) Cycling performance
(e) Rate performance of the K3V2(PO4)3 and K3V2(PO4)3/C.

The PVP/C composite's well-defined redox peaks, increased capacity, and improved charge/discharge characteristics highlight how the redox activity of the sample is boosted by the 3D porous structure and carbon addition. Fig. 6 (b-e) compares the electrochemical reactions of the blocks and $K_3V_2(PO_4)_3$/C. The $K_3V_2(PO_4)_3$/C composite demonstrates a significantly improved rate capability and cycling performance in comparison to traditional $K_3V_2(PO_4)_3$ materials. The hybrid electrode's electrochemical efficacy is substantially enhanced by the inclusion of a 3D porous carbon network. The composite attains a specific capacity of 122 mAh g^{-1} during the initial discharge at a current density of 100 mA g^{-1}. It is remarkable that it maintains 117.2 mAh g^{-1} after 100 consecutive charge–discharge cycles, which equates to a capacity retention of approximately 99.4%. This exceptional cyclic stability is indicative of the carbon framework's electrical conductivity and mechanical integrity. In addition, the composite exhibits superior long-term performance and specific capacity in comparison to other reported PVP-based cathodes, as described in Table 1 [50-56]. These results emphasize the carbon integration strategy's efficacy in enhancing the electrode

material's storage capacity and durability. This system has an initial Coulombic efficiency of 74.6%. It stabilizes at 98.5% after 50 cycles of slow climb to 97.3%. Under the same current density, the $K_3V_2(PO_4)_3$ initially delivers 108 $mAhg^{-1}$ and after 100 cycles, it retains 61.3 $mAhg^{-1}$, a capacity retention of 56.2%. This provides a consistent capacity of around 90 $mAhg^{-1}$ for 600 cycles at 200 mAg^{-1}, as shown in Fig. 6(c). On the other hand, after 100 cycles, the PVP's capacity drops below 50 $mAhg^{-1}$. The capacity retention of the PVP/C may be maintained at 93.8% after 1000 cycles at 500 mAg^{-1} (Fig. 6d). Fig. 6(e) shows that the PVP/C outperforms the blocks in terms of rate performance, as they show better capacity at all current densities evaluated, which range from 100 to 1000 mAg^{-1}.

Table 1. Performance benchmarking of electrochemical features.

Electrode samples	Discharge capacity ($mAhg^{-1}$)	Capacity retention (%)	Ref.
KVP/C	77	87.5	[50]
KVP/C	105	92.1	[51]
CNT, rGO, C integrated KVP	57	75.6	[52]
$K_3V_2(PO_4)_3/C$	119	93.4	[53]
$K_3V_2(PO_4)_2F_3$	100	92.0	[54]
$K_3V_2(PO_4)_3$	52.6	85.7	[55]
$K_3V_2(PO_4)_3/C$	122	99.4	This work

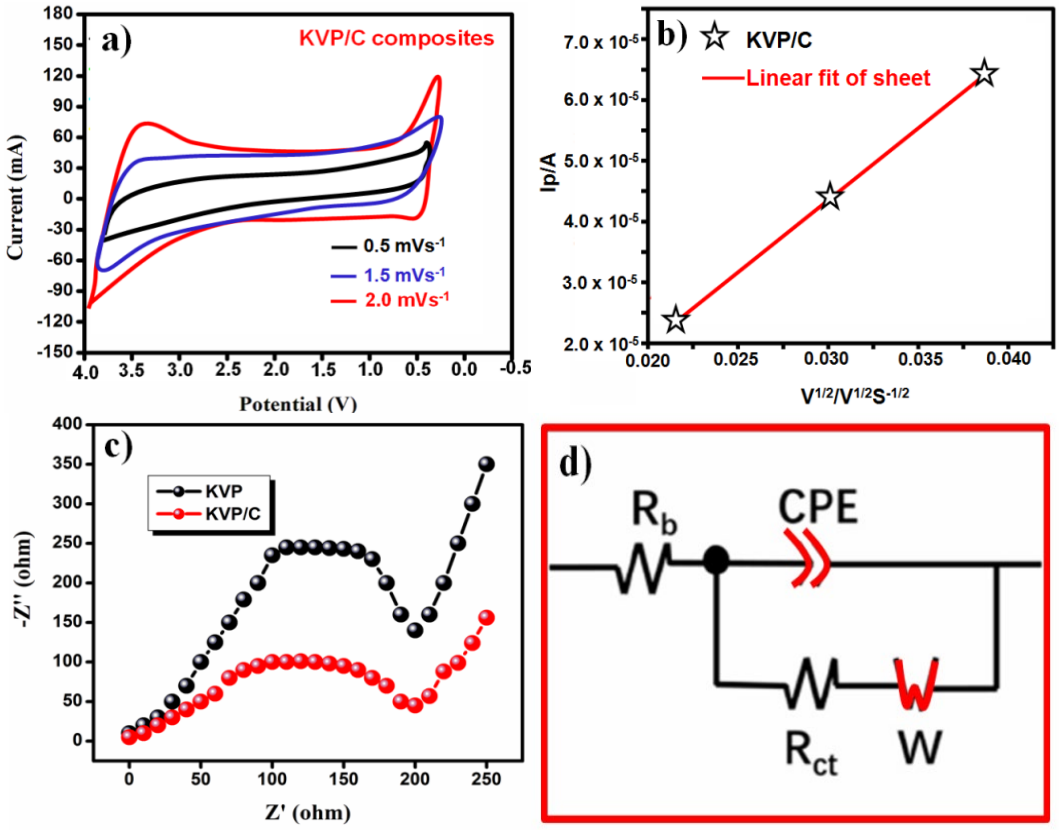

Fig. 7. (a) CV curves of the $K_3V_2(PO_4)_3/C$ (b) Cycling (c) Nyquist plot of $K_3V_2(PO_4)_3/C$; (d) equivalent circuit.

Fig. 7 illustrates the electrochemical impedance behavior and charge transfer characteristics of both PVP and its C integrated composites. The apparent diffusion coefficient (D app) of KVP is determined to be 4.1×10^{9} cm^2s^{-1}. (Fig. 7(a)). In contrast, PVP/C displays a much higher diffusion coefficient of 1.66×10^{8} cm^2s^{-1}, which is roughly four times greater than that of PVP (Fig. 7b). The conductive carbon network, which promotes quicker K^+ ion transit and enhances electrochemical performance, is responsible for this improvement in ion diffusion. Fig. 7(c) presents the EIS analysis of the PVP/C composite, highlighting its interfacial resistance and charge transfer properties.

In the Nyquist plot, the semicircle observed in the high-frequency region corresponds to the charge transfer resistance (Rct), whereas the linear portion at lower frequencies is associated with the diffusion resistance of K^+ ions, commonly represented by the Warburg element [57]. This is accomplished by fitting their kinetic behaviors to the analogous circuit model shown in Fig. 7b. As a result, the Rct values of the PVP/C and PVP are made to appear as about 101 and 245 Ω, in that order. The well-integrated carbon matrix and 3D porous structure, which promote quick ion transit and guarantee structural integrity throughout prolonged cycling, are responsible for this improved electrochemical behavior. These results demonstrate the $K_3V_2(PO_4)_3$/C composite's remarkable electrochemical benefits, which make it a promising material for next-generation potassium-ion batteries.

3.8. Photocatalytic studies

The potential use of the nanocomposites obtained was explored in the photodegradation of CR and RhB. For this investigation, the photodegradation of CR & RhB dye was monitored over time by measuring the decrease in absorbance of the characteristic peak at 498 nm & 554 nm, respectively. Only 34.5% of CR dye degradation was observed after 60 min without a photocatalyst. The degradation profile of both CR and RhB was shown in Fig. 8 (a & b). In both dye degradation, the KVP/C composite showed outstanding degradation than compared with pristine KVP. The CR and RhB degradation of KVP/C was found to be 77 and 98%, respectively, which is higher than pristine KVP (33 and 27 %, respectively). The experimental data was analyzed using two commonly used kinetic models such as I and II order to obtain insight into the photocatalytic degradation mechanism of CR [58].

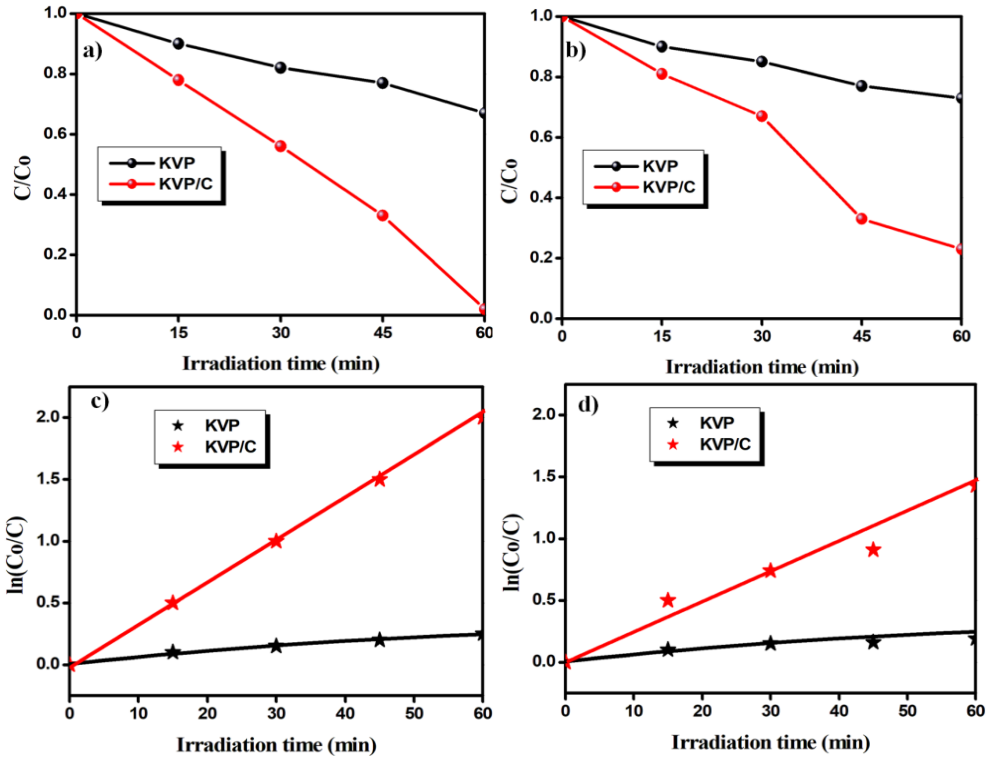

Fig. 8. Time dependent UV spectra of (a) CR (b) RhB; First order kinetic plot for rate constant determination (c) CR and (d) RhB.

These models are frequently employed to assess the reaction rate by measuring the interaction between the dye molecules and active sites on the photocatalyst surface. The degradation kinetics were evaluated using their respective linearized equations, and the results indicated a more favorable fit with the pseudo-first-order model, as indicated by the higher correlation coefficients. The rate constants for CR and RhB were calculated to be 0.00876 min^{-1} and 0.09761 min^{-1}, respectively, as shown in Fig. 8(c) and (d). These values suggest that RhB degrades at a faster rate than CR under identical conditions. Additionally, the pH of the solution is acknowledged as a critical factor that can substantially impact the generation of reactive species and the surface charge of the photocatalyst, thereby affecting the overall degradation efficiency. A series of experiments were conducted to systematically evaluate this effect, varying the pH of the reaction medium from 3 to 12, while maintaining a constant dye concentration of 10 mg L^{-1}. The results illustrated a significant correlation between pH and photocatalytic performance, underscoring the necessity of optimizing reaction conditions to obtain the highest possible degradation efficiency. The interplay between catalyst activity and solution chemistry in determining photocatalytic outcomes is emphasized by these findings.

The obtained results are shown in Fig. 9 (a). As the solution became more alkaline (pH 6 to 12), the rate of dye decomposition showed a noticeable increase. Four successive cycles of the photocatalytic process were performed to ascertain for recycling and robustness of the photocatalyst. Every cycle lasted sixty minutes under obvious irradiation. As demonstrated in Fig. 9(b), no appreciable decrease in photocatalytic activity was seen for the KVP/C photocatalyst up to four cycles. A little drop in the photocatalytic activity in the fourth cycle may be ascribed to a drop-in dye quantity in the solution resulting from dye breakdown.

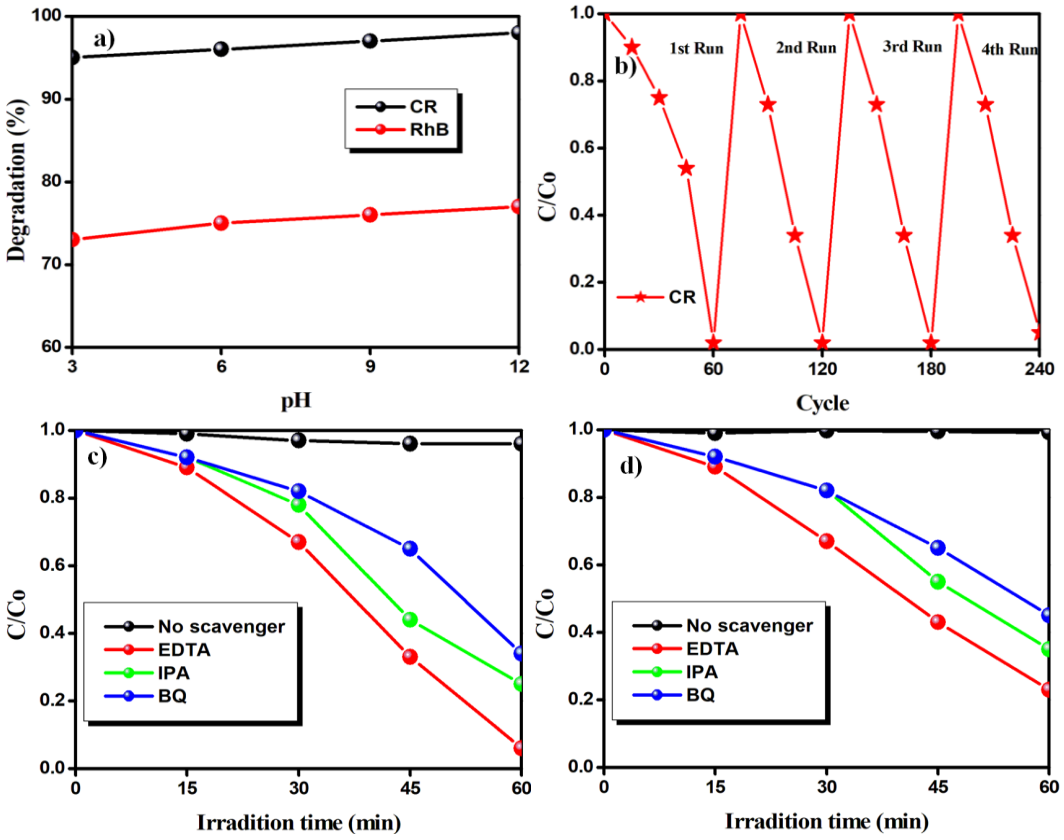

Fig. 9. (a) Effect of pH on the degradation of CR & RhB using PVP/C (b) Recycle test of KVP/C over four cycles, Scavenger test of PVP/C using (c) CR and (d) RhB dyes.

Furthermore, scavenger studies were performed to identify the reactive species involved in the photocatalytic decomposition rate of CR and RhB dyes during the involvement of the PVP/C catalyst, aiming to clarify the underlying degradation mechanism. Moreover, EDTA, IPA, and BQ were applied to quench h^+, ·OH, and $\cdot O_2^-$ radicals, thereby elucidating their roles in the photocatalytic process. The corresponding photodegradation rates and efficiencies for CR and RhB dyes are depicted in Fig. 9(c) and (d). By incorporating IPA and BQ as specific scavengers for hydroxyl (·OH) and superoxide ($\cdot O_2^-$) radicals, respectively, the impact of reactive species on the photocatalytic degradation of CR was evaluated. Upon the introduction of these scavengers, the dye removal efficacy experienced a significant decrease, decreasing from 97% to 74% with IPA and further to 45.9% with BQ. This indicates the significant involvement of these reactive oxygen species. ·OH and $\cdot O_2^-$ radicals are essential components of the oxidative degradation mechanism, as evidenced by the significant decrease in degradation performance. In addition, the data suggests that the PVP/C system's superior photocatalytic efficiency is significantly influenced by the primary oxidizing agents, which are both photogenerated holes (h^+) and hydroxyl radicals. [59].

3.9. Antioxidant property

Furthermore, the excellent antioxidant activity of the PVP/C composite was proven by the DPPH assay. The antioxidant property is shown in Fig. 10. The highest antioxidant activity exhibited by the PVP/C composite proved that the antioxidant activity is greatly enhanced due to the synergetic effects between supported PVP and C, respectively. The strong free radical scavenging ability of PVP/C suggests its potential application in biomedical and pharmaceutical fields. The synergistic interaction between PVP and carbon enhances electron transfer, effectively neutralizing ROS and preventing oxidative damage. This outstanding antioxidant performance makes PVP/C a promising candidate for antioxidant-based therapies, drug delivery, and biomedical formulations. Hence this study concludes that the PVP/C composite synthesized using microwave assisted technique can be an excellent candidate for biomedical, pharmaceutical as well as other industrial applications. The PVP/C composite exhibits excellent potential for energy storage, wastewater treatment and biomedical applications, owing to its superior electrochemical stability, photocatalytic efficiency, and antioxidant properties. Its multifunctionality makes it a promising material for next-generation batteries, environmental remediation and pharmaceutical formulations.

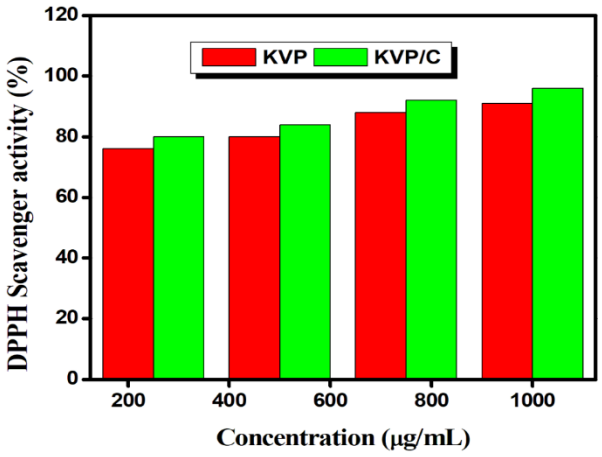

Fig. 10. Antioxidant results of PVP/C in terms of % DPPH.

4. Conclusion

To summarize, we have successfully synthesized new PVP/C composites utilizing a cost-efficient microwave irradiation approach. The synthesized PVP/C composite, characterized by a three-dimensional porous structure, exhibited superior electrochemical performance, achieving an initial specific capacity of 122 mAh g^{-1} at a current density of 100 mA g^{-1}. Significantly, the material maintained 99.0% of its capacity after 2000 continuous cycles at an elevated current density of 1000 mA g^{-1}, demonstrating exceptional long-term stability. The exceptional performance results from the synergistic effects of the porous structural framework and the conductive carbon coating, which together increase surface area, promote fast ion movement, and ensure efficient electron conduction. The results validate the composite's significant potential as a dependable and efficient cathode material for potassium-ion batteries, rendering it particularly appealing for forthcoming large-scale energy storage applications.

The PVPC composite demonstrated exceptional photocatalytic activity in addition to its electrochemical advantages. It achieved a 98.5% degradation efficiency of CR dye with a corresponding rate constant of 0.09761 min^{-1}, surpassing its activity against RhB under identical conditions. In order to gain a more comprehensive understanding of the degradation mechanism, the role of reactive species and the impact of pH on degradation efficiency were systematically investigated through scavenger studies. Future research into the application of this composite in biomedical disciplines, including drug delivery, wound healing, and prospective anticancer therapies, is enabled by its inherent antioxidant behavior, which is a result of its multifunctional properties. In addition, it will be essential to assess the cost-effectiveness and scalability of the synthesis process in order to transition this material from laboratory-scale development to commercial implementation in a variety of industrial sectors.

Data acknowledgements

The author(s) received no financial support for the research, authorship, and/or publication of this article.

Conflicts of interest

The authors declare no competing financial interest.

Availability statement

All data analysed during the study are included in this article and will be made upon reasonable request.

Author contribution statement

G.P., contributed to the conceptualization, methodology and original manuscript preparation, as well as its review and final editing. S.P.M., performed data curation. R.G.R., performed data validation. D.P., performed verification of experimental results.

Funding

No funding obtained for this study.

References

[1] X. Wu, Z. Han, X. Zheng, S. Yao, X. Yang, T. Zhai, Nano Energy **31**, 410 (2017); https://doi.org/10.1016/j.nanoen.2016.11.035
[2] Hong, D., Zang, W., Guo, X., Fu, Y., He, H., Sun, J., Xue, X., ACS applied materials & interfaces, **8**(33), 21302 (2016); https://pubs.acs.org/doi/abs/10.1021/acsami.6b05252
[3] Simon, P., Gogotsi, Y., Dunn, B., Science, **343**(6176), 1210 (2014); https://doi.org/10.1126/science.1249625
[4] Yi, H., Huang, D., Qin, L., Zeng, G., Lai, C., Cheng, M., Guo, X., Applied Catalysis B: Environmental, **239**, 408(2018); https://doi.org/10.1016/j.apcatb.2018.07.068
[5] Qu, L., Zhao, Y., Khan, A.M., Han, C., Hercule, K.M., Yan, M., Liu, X., Chen, W., Wang, D., Cai, Z. Xu, W., Nano letters, **15**(3), 2037 (2015); https://pubs.acs.org/doi/abs/10.1021/nl504901p
[6] Larcher, D., Tarascon, J. M., Nature chemistry, **7**(1), 19 (2015); https://doi.org/10.1038/nchem.2085
[7] Yabuuchi, N., Kajiyama, M., Iwatate, J., Nishikawa, H., Hitomi, S., Okuyama, R., Komaba, S. Nature materials, **11**(6), 512 (2012); https://doi.org/10.1038/nmat3309
[8] Wang, X., Xu, X., Niu, C., Meng, J., Huang, M., Liu, X., Mai, L., Nano letters, **17**(1), 544 (2017); https://doi.org/10.1021/acs.nanolett.6b04611
[9] Recham, N., Rousse, G., Sougrati, M. T., Chotard, J. N., Frayret, C., Mariyappan, S., Tarascon, J. M. (2012), Chemistry of Materials, 24(22), 4363-4370; https://doi.org/10.1021/cm302428w
[10] Hironaka, Y., Kubota, K., Komaba, S., Chemical Communications, **53**(26), 3693 (2017); https://doi.org/10.1039/C7CC00806F
[11] Vaalma, C., Giffin, G. A., Buchholz, D., Passerini, S., Journal of the Electrochemical Society, **163**(7), A1295 (2016); https://doi.org/10.1149/2.0921607jes
[12] Rui, X., Sim, D., Wong, K., Zhu, J., Liu, W., Xu, C., Yan, Q., Journal of Power Sources, **214**, 171(2012); https://doi.org/10.1016/j.jpowsour.2012.03.113
[13] Rui, X. H., Li, C., Chen, C. H., Electrochimica Acta, **54**(12), 3374(2009); https://doi.org/10.1016/j.electacta.2009.01.011
[14] Rui, X. H., Li, C., Liu, J., Cheng, T., Chen, C. H., Electrochimica Acta, **55**(22), 6761(2010); https://doi.org/10.1016/j.electacta.2010.05.093
[15] Rui, X., Sun, W., Wu, C., Yu, Y., Yan, Q., Advanced Materials (Deerfield Beach, Fla.), **27**(42), 6670(2015); https://doi.org/10.1002/adma.201502864
[16] Hong, S. Y., Kim, Y., Park, Y., Choi, A., Choi, N. S., Lee, K. T., Energy & Environmental Science, **6**(7), 2067 (2013); https://doi.org/10.1039/C3EE40811F
[17] Han, J., Li, G. N., Liu, F., Wang, M., Zhang, Y., Hu, L., Xu, M., Chemical Communications, **53**(11), 1805 (2017); https://doi.org/10.1039/C6CC10065A
[18] Liu, T., Wang, B., Gu, X., Wang, L., Ling, M., Liu, G., Zhang, S., Nano Energy, **30,** 756 (2016); https://doi.org/10.1016/j.nanoen.2016.09.024
[19] Islam, S., Alfaruqi, M.H., Putro, D.Y., Mathew, V., Kim, S., Jo, J., Kim, S., Sun, Y.K., Kim, K., Kim, J., ChemSusChem, **11**(13) .2239 (2018); https://doi.org/10.1002/cssc.201800724
[20] Cao, J., Wang, Y., Wang, L., Yu, F., Ma, J., Nano letters, **19**(2), 823 (2019); https://doi.org/10.1021/acs.nanolett.8b04006
[21] Zhang, L., Zhang, B., Wang, C., Dou, Y., Zhang, Q., Liu, Y., Liu, H. K., Nano Energy, **60**, 432 (2019); https://doi.org/10.1016/j.nanoen.2019.03.085
[22] Han, J., Li, G. N., Liu, F., Wang, M., Zhang, Y., Hu, L., Xu, M., Chemical Communications, **53**(11), 1805 (2017); https://doi.org/10.1039/C6CC10065A
[23] Bianchini, M., Fauth, F., Brisset, N., Weill, F., Suard, E., Masquelier, C., Croguennec, L., Chemistry of Materials, **27**(8), 3009 (2015); https://doi.org/10.1021/acs.chemmater.5b00361
[24] Matts, I. L., Dacek, S., Pietrzak, T. K., Malik, R., Ceder, G., Chemistry of Materials, **27**(17), 6008 (2015); https://doi.org/10.1021/acs.chemmater.5b02299.
[25] Zhang, B., Dugas, R., Rousse, G., Rozier, P., Abakumov, A. M., Tarascon, J. M., Nature communications, **7**(1), 10308 (2016); https://doi.org/10.1038/ncomms10308
[26] Chen, N., Zhou, J., Kang, Q., Ji, H., Zhu, G., Zhang, Y., Hou, W., Journal of Power Sources, **344**, 185 (2017); https://doi.org/10.1016/j.jpowsour.2017.01.119

[27] Xu, J., Dou, S., Cui, X., Liu, W., Zhang, Z., Deng, Y. Chen, Y., Energy Storage Materials, **34**, 85 (2021); https://doi.org/10.1016/j.ensm.2020.09.001
[28] Liu, P., Zhu, K., Gao, Y., Luo, H., Lu, L., Advanced Energy Materials, **7**(23), 1700547 (2017); https://doi.org/10.1002/aenm.201700547
[29] Guo, J., Liang, J., Yuan, X., Jiang, L., Zeng, G., Yu, H., Zhang, J., Chemical Engineering Journal, **352**, 782 (2018); https://doi.org/10.1016/j.cej.2018.07.071
[30] Tartaya, S., Bagtache, R., Djaballah, A. M., Özacar, M., Trari, M., Journal of Materials Science: Materials in Electronics, **32**(11),15441 (2021); https://doi.org/10.1007/s10854-021-06093-0
[31] Liu, Z., Sun, K., Wei, M., Ma, Z,, Journal of Colloid and Interface Science, 531, 618 (2018); https://doi.org/10.1016/j.jcis.2018.07.077
[32] Hu, B., Xu, C., Yu, D., Chen, C., Journal of Colloid and Interface Science, **590**, 341 (2021); https://doi.org/10.1016/j.jcis.2021.01.042
[33] Bi, Z., Wang, W., Zhao, L., Wang, X., Xing, D., Zhou, Y., Chen, C., Environmental Research, 119592 (2024); https://doi.org/10.1016/j.envres.2024.119592
[34] Fan, X., Fu, Q., Liu, G., Jia, H., Dong, X., Li, Y. F., Cui, S., Environmental Science and Ecotechnology, **22** 100469 (2024); https://doi.org/10.1016/j.ese.2024.100469
[35] Singh, N., Sherin, G. R., Mugesh, G., Angewandte Chemie, **135**(33), e202301232 (2023); https://doi.org/10.1002/ange.202301232
[36] Alagarsamy, S., Mariappan, K., Chen, S. M., Ramachandran, R., Devanesan, S., AlSalhi, M. S., Chuang, H. Y., FlatChem, **42**, 100563 (2023); https://doi.org/10.1016/j.flatc.2023.100563
[37] Jenkins, T., Alarco, J. A., Mackinnon, I. D., ACS omega, **6**(3), 1917 (2021); https://doi.org/10.1021/acsomega.0c04675
[38] Gokulakrishnan, N., Pandurangan, A., Sinha, P. K., Industrial & Engineering Chemistry Research, **48**(3), 1556 (2009); https://doi.org/10.1021/ie800907y
[39] Guo, S., Bai, Y., Geng, Z., Wu, F., Wu, C., Journal of Energy Chemistry, **32**, 159 (2019); https://doi.org/10.1016/j.jechem.2018.07.011
[40] Han, J., Li, G. N., Liu, F., Wang, M., Zhang, Y., Hu, L. Xu, M., Chemical Communications, **53**(11), 1805 (2017); https://doi.org/10.1039/C6CC10065A
[41] Wang, E., Chen, M., Liu, X., Liu, Y., Guo, H., Wu, Z., Dou, S. X., Small Methods, **3**(4), 1800169 (2019); https://doi.org/10.1002/smtd.201800169
[42] Zhao, L., Zhao, H., Wang, J., Zhang, Y., Li, Z., Du, Z., Hou, Y., ACS applied materials & interfaces, **13**(7), 8445 (2021); https://doi.org/10.1021/acsami.0c21861
[43] BoopathiRaja, R., Parthibavarman, M., Journal of Alloys and Compounds, **811**, 152084 (2019); https://doi.org/10.1016/j.jallcom.2019.152084
[44] BoopathiRaja, R., Parthibavarman, M., Begum, A. N., Vacuum, **165**, 96 (2019); https://doi.org/10.1016/j.vacuum.2019.04.013
[45] BoopathiRaja, R., Parthibavarman, M., Electrochimica Acta, **346**, 136270 (2020); https://doi.org/10.1016/j.electacta.2020.136270
[46] BoopathiRaja, R., Parthibavarman, M., Chemical Physics Letters, **755**, 137809 (2020); https://doi.org/10.1016/j.cplett.2020.137809
[47] Jayashree, M., Parthibavarman, M., Prabhakaran, S., Ionics, **25**, 3309 (2019). https://doi.org/10.1007/s11581-019-02859-z
[48] Li, S., Kang, E. T., Neoh, K. G., Ma, Z. H., Tan, K. L., Huang, W., Applied surface science, **181**(3-4), 201 (2001); https://doi.org/10.1016/S0169-4332(01)00397-X
[49] Silversmit, G., Depla, D., Poelman, H., Marin, G. B., De Gryse, R., Journal of Electron Spectroscopy and Related Phenomena, **135**(2-3), 167 (2004); https://doi.org/10.1016/j.elspec.2004.03.004
[50] Han, J., Li, G. N., Liu, F., Wang, M., Zhang, Y., Hu, L. Xu, M., Chemical Communications, **53**(11), 1805 (2017); https://doi.org/10.1039/C6CC10065A
[51] Kuai, H. X., Lu, J. F., Lv, X. Y., Long, Y. F., Wen, Y. X., Ionics, **28**(8), 3817 (2022); https://doi.org/10.1007/s11581-022-04612-5
[52] Xianghua Zhang, Xinyi Kuang, Hanwen Zhu, Ni Xiao, Qi Zhang, Xianhong Rui, Yan Yu, Shaoming Huang, Surfaces, **3**(1), 1 (2020); https://doi.org/10.3390/surfaces3010001

[53] Xuanpeng Wang, Chaojiang Niu, Jiashen Meng, Ping Hu, Xiaoming Xu, Xiujuan Wei, Liang Zhou, Kangning Zhao, Wen Luo, Mengyu Yan, Liqiang Mai, Adv. Energy Mater. **5** (17) 1500716 (2015); https://doi.org/10.1002/aenm.201500716
[54] Xiuyi Lin, Jiaqiang Huang, Hong Tan, Jianqiu Huang, Biao Zhang, Energy Storage Materials **16**, 97 (2019); https://doi.org/10.1016/j.ensm.2018.04.026
[55] Shuai Zheng, Siqi Cheng, Shunhua Xiao, Lizhen Hu, Zhuo Chen, Bin Huang, Qingquan Liu, Jianwen Yang, Quanqi Chen, Journal of Alloys and Compounds. **815,** 152379 (2020); https://doi.org/10.1016/j.jallcom.2019.152379
[56] H.-G. Jung, J. Hassoun, J.-B. Park, Y.-K. Sun, B. Scrosat, Nat. Chem. **4**(7), 579 (2012); https://doi.org/10.1038/nchem.1376
[57] J. Yu, X. Zhou, D. Li, X. Cheng, F. Liu, Y. Yan, Adv. Energy Mater. **8**(16), 1800068 (2018); https://doi.org/10.1002/aenm.201800068
[58] M.L. Matias, A. Pimentel, A.S. Reis-Machado, J. Rodrigues, J. Deuermeier, E. Fortunato, R. Martins, et al., Nanomaterials **12** (6), 1005 (2022); https://doi.org/10.3390/nano12061005
[59] L. Sun, Q. Shao, Y. Zhang, H.Y. Jiang, S.S. Ge, S.Q. Lou, J. Lin, J.X. Zhang, et al., J. Colloid Interface Sci. **565**, 142 (2020); https://doi.org/10.1016/j.jcis.2019.12.107